Neuron, Volume *83*

Supplemental Information

Pyramidal Cell-Interneuron Interactions Underlie Hippocampal Ripple Oscillations

Eran Stark, Lisa Roux, Ronny Eichler, Yuta Senzai, Sebastien Royer, and György Buzsáki

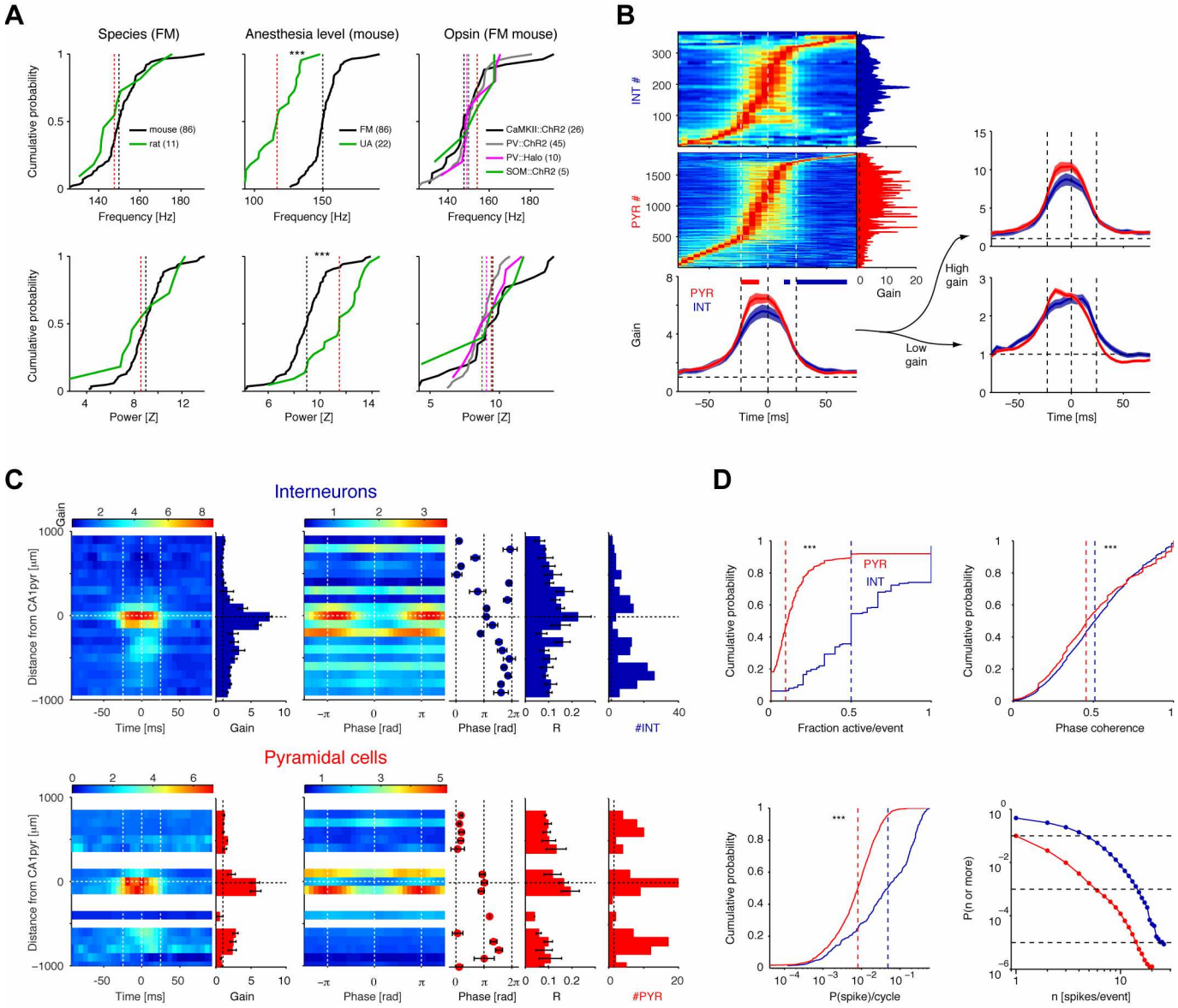

Figure S1. Properties of spontaneous LFP ripples and accompanying spiking dynamics, related to Figure 1

(**A**) Ripple properties are similar regardless of species and genotype. Data includes only sessions with ≥100 ripples (total of 115,204 ripples from 123 recording sessions in 40 animals). Each panel shows the cumulative distribution of session medians; e.g., in the top left panel, 86 sessions from freely-moving (FM) mice and 11 sessions from FM rats are included. ***, p<0.005, Kruskal-Wallis test; only significant (p<0.05) comparisons are indicated. Vertical dashed lines show group medians. While ripple frequency and power do not depend on species (mouse/rat) or the exogenous opsin expressed, ripples recorded in urethane-anesthetized (UA) mice are slower (median, 117 Hz) than in FM mice (150 Hz; p<0.001, KW test; Ylinen et al., 1995) and have higher power (11.5 vs. 9 SD; p<0.001).

(**B**) PYR and INT spiking is modulated differently during ripples. Each line corresponds to the ripple-triggered histogram of one cell, scaled (0-1), color-coded (blue-red), and sorted by the peak firing relative to the ripple power maximum (369 INT and 1869 PYR recorded during 86,845 ripple events in 87 sessions from 19 freely-behaving mice and three rats using 20-µm spacing silicon probes). Bottom, population mean±SEM expressed as

gain; only cells with peak firing-rate during ripple are included (247 INT, 1193 PYR). Vertical dashed lines indicate the span of the mean ripple event. Red/blue bars indicate times during which PYR/INT gain is higher ($p<0.05$, Bonferroni-corrected Mann-Whitney U-test). Right: Low gain PYR decrease their firing rate after ripples. Data are the same as at left, partitioned into two by the median gain (INT: 4.9; PYR: 5.5).

(**C**) SPW-ripple events are accompanied by phase-locked spiking in multiple hippocampal regions. Data are from four freely-moving mice equipped with 32-site linear probes in the right dorsal hippocampus. Ripple-triggered spike histograms (left), phase histograms (center), and depth distribution of recorded cells (right) are shown. Each line corresponds to the mean color-coded gain histogram of all PYR or INT recorded at a given distance from the center of the CA1 pyramidal layer (100 μm bins; 176 INT and 170 PYR recorded during 26 sessions). While gain indicates the overall modulation of spiking during SPW-ripple events, the resultant vector length R indicates the extent of phase locking to individual ripple cycles; note that spiking may be increased/decreased, phase modulated, or both. Bars, mean±SEM.

(**D**) Population synchrony (top) and single-unit spiking probability (bottom) during ripples (same dataset as in **B**). Top left: distribution of the number of PYR (or INT) that spike at least once during a single ripple event. Top right: distribution of the circular resultant length of the phases of all simultaneously-recorded cells (PYR or INT). Bottom left: distribution of the probability for a given cell to spike during a single ripple cycle. Bottom right: probability of a given cell to spike n or more times during a single ripple event. ***: $p<0.005$, U-test.

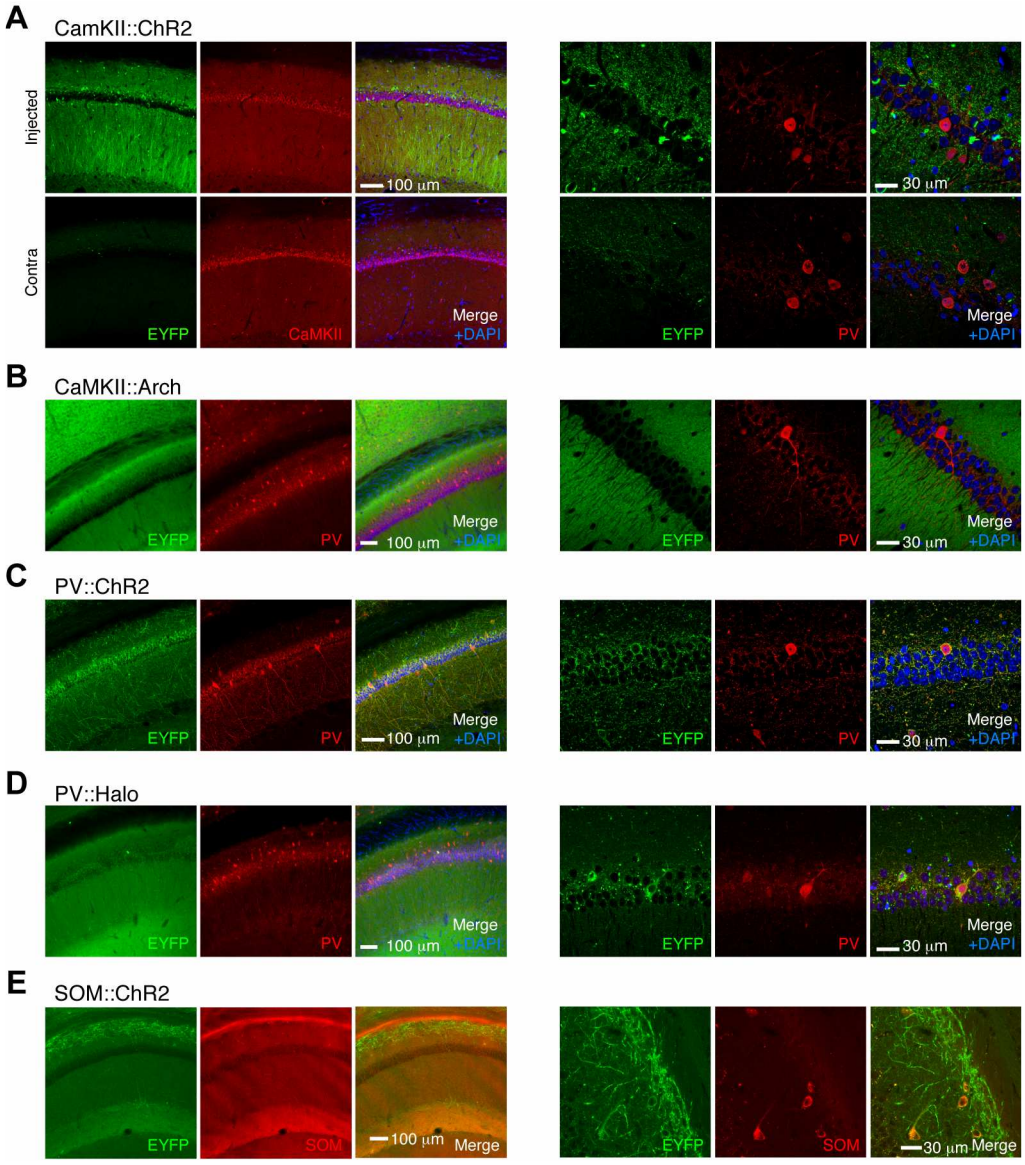

Figure S2. Opsin expression in CA1 pyramidal cells and interneuron subtypes, related to Figure 2

Low (left) and high (right) magnification images of the hippocampus CA1 region in opsin-expressing rodents. In all panels, EYFP (green) is used as a reporter gene for opsin expression, cell-type specific staining is shown in red, and DAPI (blue) is used to counter-stain cell nuclei.

(**A**) Expression of EYFP in a rat injected unilaterally with rAAV5/CamKIIa-hChR2(h134R)-EYFP virus. In this case, expression of EYFP and ChR2 is driven by the CaMKIIa excitatory cell promoter. Immunostaining for CaMKIIa (red, left) is strongest in the CA1 pyramidal cell layer, while immunostaining for PV (red, right), a marker for a major subpopulation of interneurons, does not co-localize with EYFP.

(**B**) Expression of EYFP in a CaMKII::Arch transgenic mouse (CaMKII-Cre::Ai35D). Immunostaining for PV does not co-localize with EYFP.

(**C**) Expression of EYFP in a PV::ChR2 transgenic mouse (PV-Cre::Ai32), where EYFP and ChR2 expression are driven by the PV gene promoter. In this case, immunostaining for PV co-localizes with EYFP.

(**D**) Co-localization of EYFP with PV immunostaining is also observed in the PV::Halo transgenic mouse (PV-Cre::Ai39).

(**E**) EYFP co-localizes with SOM immunostaining (red) in the SOM::ChR2 transgenic mouse (SOM-Cre::Ai32).

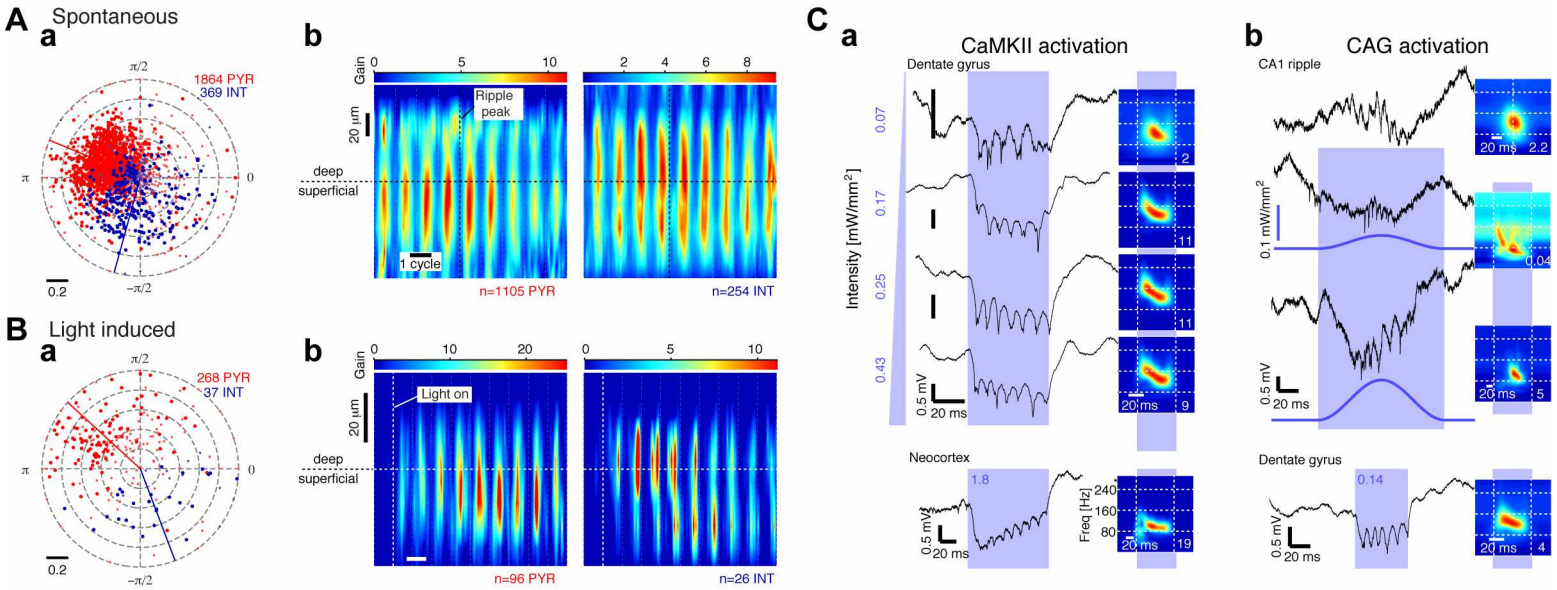

Figure S3. Properties of iHFOs and accompanying spiking dynamics, related to Figure 3

(**A**) Spiking during spontaneous ripples. (**Aa**) PYR spiking (red) precedes INT spiking (blue) by approximately 90°. Each dot shows the preferred phase of spiking for a single unit. Larger dots indicate phase-modulated units ($p<0.05$, Rayleigh test) and colored lines show mean phase of those units. (**Ab**) Superficial PYR have higher gain than deep PYR on every ripple cycle. Color-coded maps show spiking gain, resolved by the phase of the spontaneous ripple (abscissa; see also **Figure 3A**) and the depth in the CA1 pyramidal layer (ordinate; see also **Figure 3B**). Superficial PYR have higher gain than deep PYR ($p<0.001$, U-test), and spatiotemporal dynamics differ between PYR and INT.

(**B**) PYR spiking precedes INT spiking also during iHFOs induced at threshold intensity, and similar spatiotemporal dynamics are apparent also during iHFOs (see also **Figure 3C** and **3D**).

(**C**) HFOs can be induced in multiple cortical regions. (**Ca**) HFOs induced by CaMKII::ChR2 activation in dentate gyrus (DG) and neocortex. Top: wide-band traces (1-5000 Hz; left) and time-frequency decomposition of DG recordings from a freely-moving rat during single-shank illumination with light pulses of increasing intensities (indicated by numbers at left; 0.07-0.43 mW/mm^2 at the recording location). In all spectrograms, each averaged over ≥10 light pulses, numbers at bottom-right indicate peak power (Z-score, normalized by SWS power in the absence of light). Induced frequency and power are intensity dependent. Bottom: single-shank illumination in neocortical layer 5 (freely-moving mouse) also induces HFOs. (**Cb**) HFOs induced by pan-neuronal activation (CAG::ChR2) in CA1 (top) and DG (bottom). In CA1 (recording from a freely-moving wild-type rat), ripples induced by pan-neuronal activation are intensity-dependent and resemble the spontaneous events. Pan-neuronal ripples can also be induced in the DG (recording from a different rat). HFOs were induced in all CaMKII::ChR2 animals (DG, two rats; neocortex, two rats and four freely-moving mice) and in all three CAG::ChR2 rats tested.

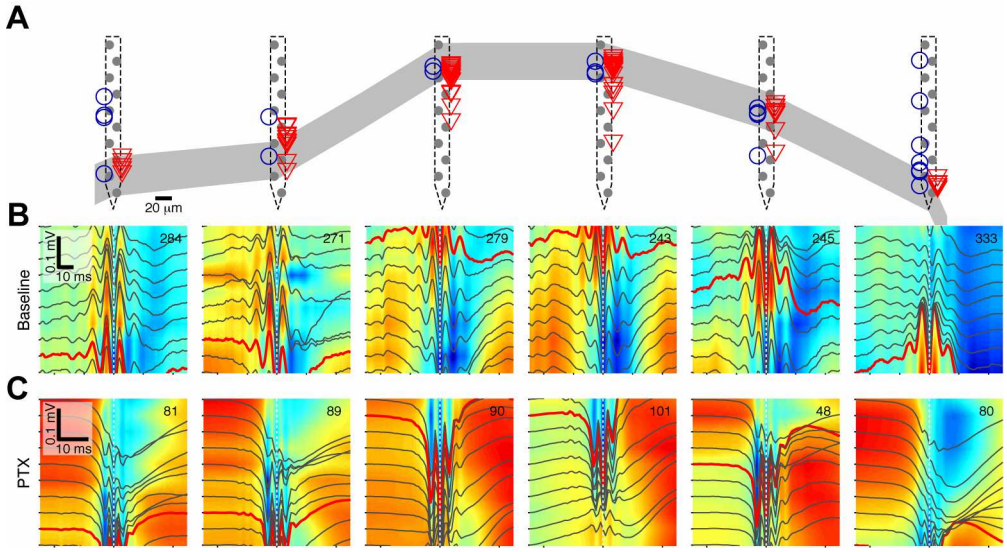

Figure S4. Spontaneous "fast ripples" during $GABA_A$ receptor blockade, related to Figure 4

Experimental design and dataset are the same as in **Figure 4C**, but this figure depicts spontaneous ripples (rather than light-induced HFOs) in the spatiotemporal (rather than spectrotemporal) domain.

(**A**) Schematic of six-shank probe, drawn to scale with sites of peak ripple power indicated by gray line (corresponding to the site of the red traces in **B**), and estimated location of INT and PYR somata shown by blue circles and red triangles, respectively.

(**B**) LFP traces (gray lines) averaged over all spontaneous ripples (80-250 Hz; aligned by ripple peak power, vertical dashed line) before drug injection, superimposed on maps interpolated linearly from the voltage traces. Each trace corresponds to the mean voltage recorded at one site, the red traces mark the center of the CA1 pyramidal cell layer, and the number of events is indicated for each shank.

(**C**) LFP traces averaged over all "fast ripples" (200-300 Hz) that occurred spontaneously after PTX injection (none occurred before). Note expanded abscissa relative to panel **B**. Compared to the no-drug physiological ripples, epileptic "fast ripples" are shorter and ride on a str. pyramidale large negative wave (interictal spike). Similar LFP patterns were observed in all experiments.

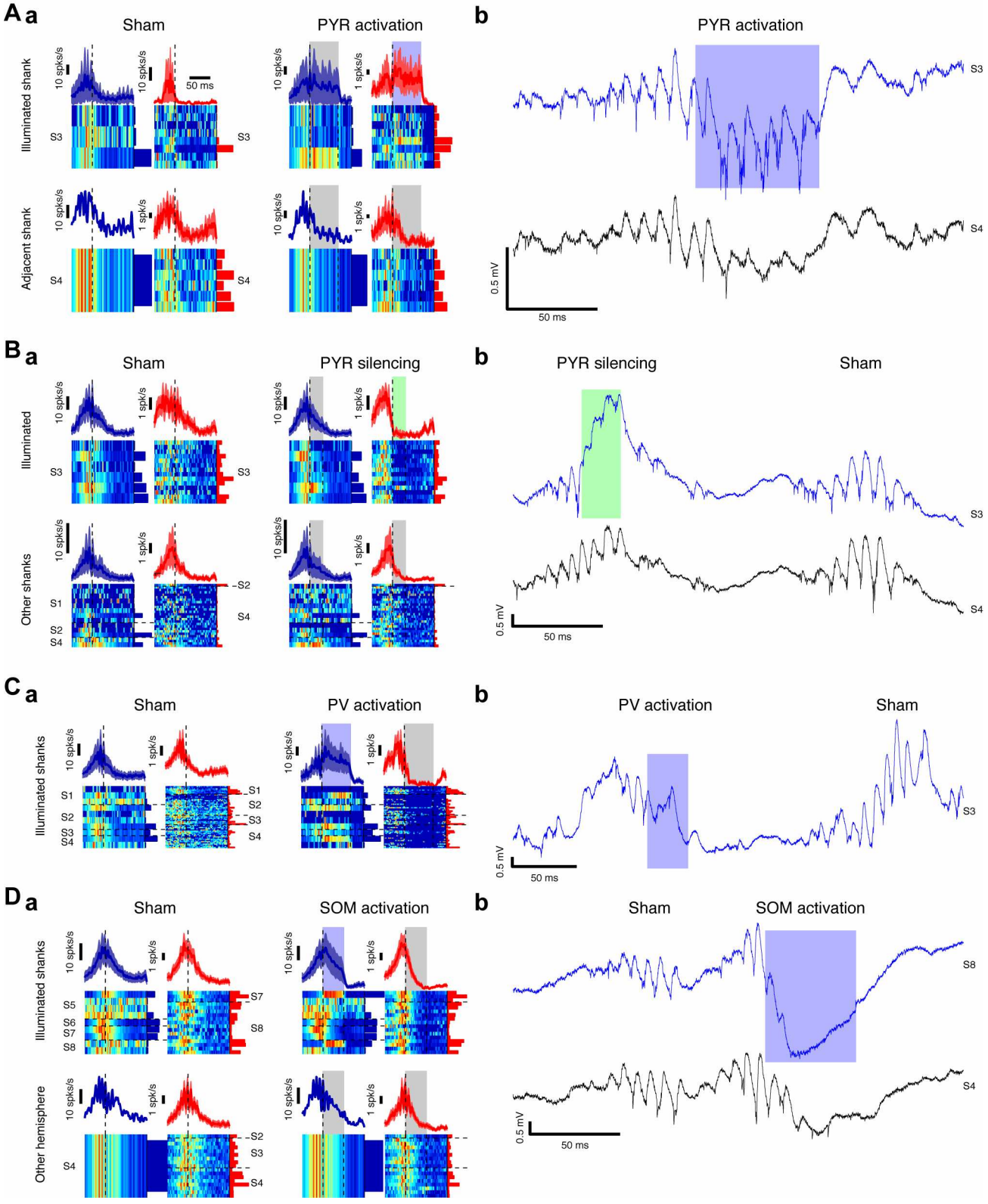

Figure S5. Closed-loop control of local spiking during LFP ripples, related to Figure 5

(**Aa**) PYR activation (CaMKII::ChR2, as in **Figure 5C**). Here, spiking is shown for both sham and closed-loop trials, and separately for the illuminated shank (S3, top right) and other shanks. Each line in the color-coded plots shows the peri-ripple time histogram for one unit, scaled 0 to 1 and color-coded blue to red; bars at right show the relative peak rate for each cell. Vertical dashed lines show the time of peak ripple power, and horizontal dashed lines separate groups of units recorded on distinct shanks (indicated with text only during sham condition). Light activation results in localized PYR activity on S3 but much less on the adjacent S4. (**Ab**) Wide-band (1-5000 Hz) traces during a single closed-loop stimulation event. Blue trace is for the illuminated shank (S3) and black trace is for an adjacent shank (S4). Note that the spontaneous ripple is evident on both shanks but the closed-loop iHFO is localized to S3.

(**Ba**) Direct PYR silencing via CaMKII::Arch (as in **Figure 5D**). Here, illumination silences PYR activity on S3 but much less on other shanks. (**Bb**) Wide-band traces during a single closed-loop event followed by a sham event. The LFP disruption is localized to the illuminated shank.

(**Ca**) Indirect PYR silencing via PV interneuron activation (same data as in **Figure 5E**). Interneuron spiking is prolonged and PYR spiking is suppressed. (**Cb**) Wide-band trace from one shank during closed-loop ripple disruption followed by a sham event.

(**Da**) Indirect PYR silencing via SOM interneuron activation (same data as in **Figure 5F**). PYR are silenced on the illuminated but not in the contralateral CA1 of a bilaterally implanted mouse. (**Db**) Wide-band traces during a sham event followed by a closed-loop event. Note the specificity of ripple disruption to the illuminated CA1.

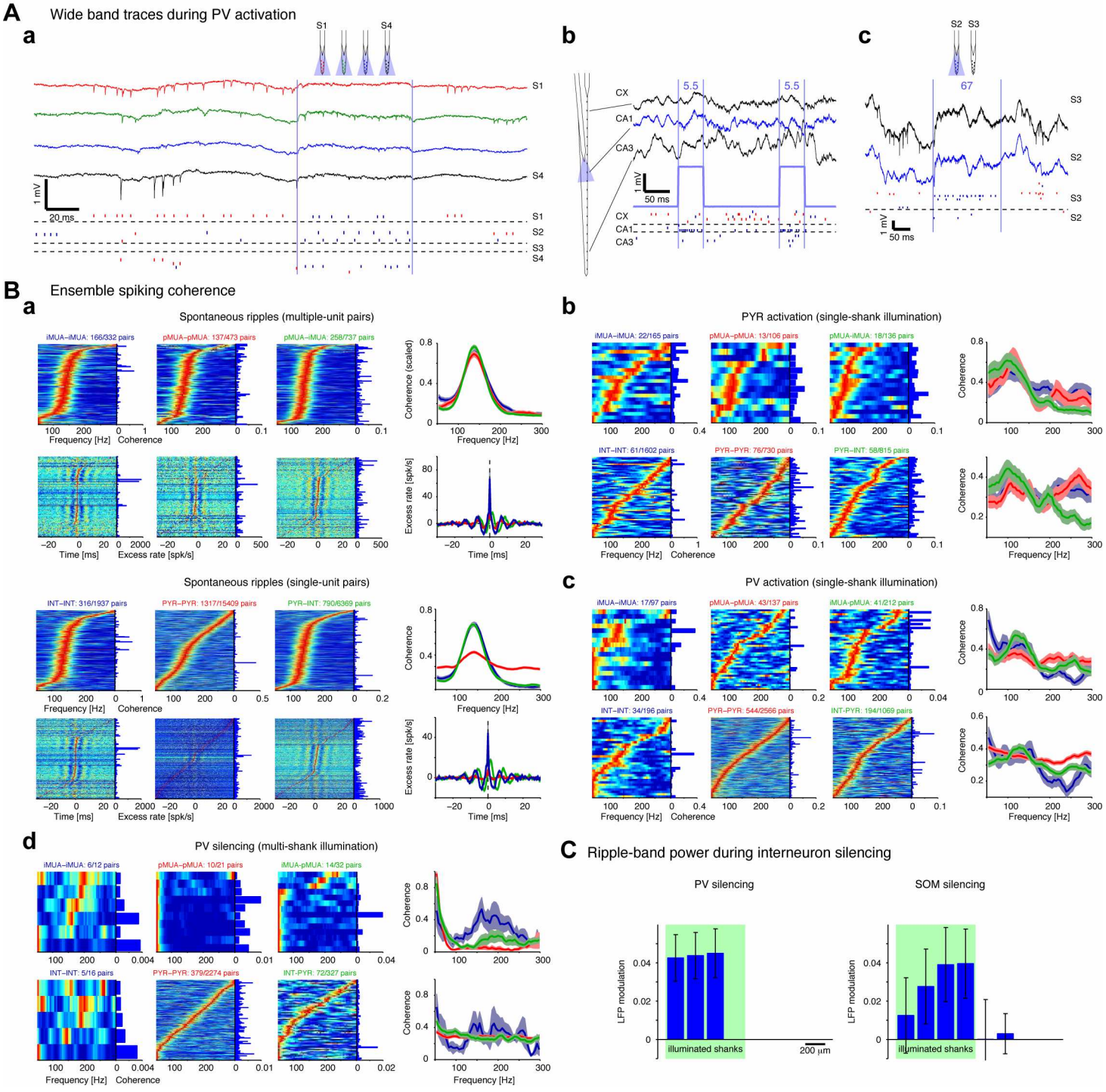

Figure S6. PV activation does not generate iHFOs but can pace ensemble spiking, related to Figure 6

(**A**) PV activation does not generate iHFOs. (**Aa**) Wide-band (1-5000 Hz) traces during multi-site square pulse illumination are shown (light intensity: 1-1.5 mW/mm^2; freely-moving PV::ChR2 mouse). In all panels, vertical blue lines delimit illumination, horizontal dashed lines separate units recorded on distinct shanks, PYR spiking is indicated by red ticks, and INT spiking is indicated by blue ticks (see also **Figure 6A**). Note induced PV spiking, suppressed PYR spiking, and no induced LFP ripples. (**Ab**) Recording from a freely-moving mouse implanted

with a 32-site linear probe equipped with two 405 nm laser diodes (LDs) while CA1 pyramidal layer was illuminated via the CA1 LD (light intensity at the CA1 channel, 5.5 mW/mm^2). Note increased spiking of CA1 PV and suppression of CA1 PYR spiking upon illumination. (**Ac**) Wide-band traces from a urethane-anesthetized mouse implanted with a high-density probe equipped with an optical fiber coupled to an external 473 nm DPSSL. Upon illumination with super-high intensity light (67 mW/mm^2), note increased INT spiking on both shanks and suppressed PYR spiking. iHFOs were not observed in any configuration (seven freely-moving mice and six urethane-anesthetized mice).

(**B**) PV interneurons can pace ensemble spiking activity. (**Ba**) Ensemble spiking during spontaneous ripples exhibits synchronous oscillations. Top panels show cross-shank spiking coherence and correlations for pairs of agglomerated spike trains, and bottom panels show coherence for pairs of individual spike trains (the spikes are the same in all cases). Only pairs with significant ($p<0.05$, Bonferroni-corrected F-test; data from 21 awake-behaving mice and four rats) are included. Cross-correlation histograms (CCH) were corrected to indicate excess spiking (convolution predictor, ±5 ms). Coherence (and CCH) values were scaled 0-1, color-coded blue-red, and sorted according to frequency (or time) of peak; bars at right of each panel indicates the peak un-scaled values, and bands at far right show mean±SEM. While the estimate based on single-units is relatively noisy, especially for PYR-PYR pairs, the estimate based on agglomerated spike trains is more clearly expressed in the ripple band. All spike train pairs are rhythmic ($p<0.05$, Bonferroni-corrected F-test). (**Bb**) Similar analysis during single-shank PYR activation (data from four freely-moving CaMKII::ChR2 mice and one rat). For both single-unit and agglomerated spike trains, PYR-INT trains (green bands) are coherent at the ripple frequency. (**Bc**) During PV activation (single-shank illumination; five freely-moving PV::ChR2 mice), INT spiking is increased (reflected by low-frequency coherence between some INT pairs; blue bands) and paces PYR spiking on other shanks (green bands). (**Bd**) Similar analysis during four-shank PV silencing (four head-fixed PV::Halo mice). PYR spiking is increased, evident as low-frequency coherence between most pMUA-pMUA pairs.

(**C**) LFP ripple power is increased during interneuron silencing. LFP modulation, mean ripple-band (80-250 Hz) power during multi-shank illumination (≥50 pulses, 1 s) minus the power during randomized duration-matched epochs, divided by the sum (see also **Figure 5**). Data are from 3 shanks in one PV::Halo mouse ($p<0.01$ for all 3 shanks; Mann-Whitney U-test) and from 10 shanks in two SOM::Halo mice ($p<0.01$ for 6/8 illuminated shanks).

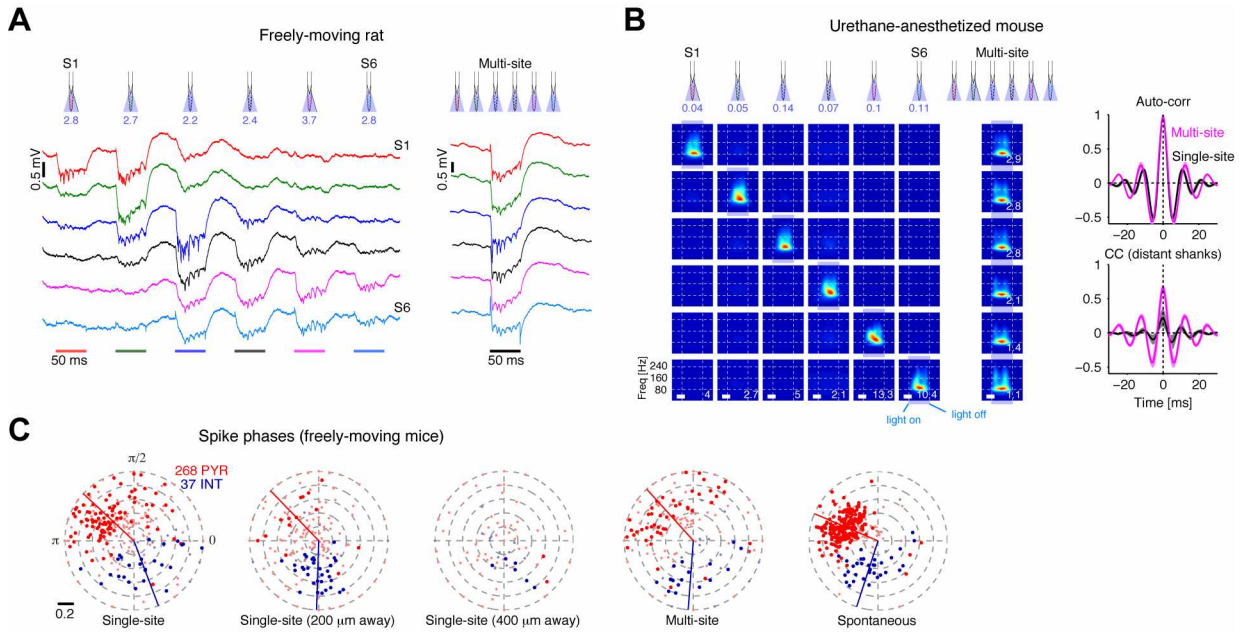

Figure S7. Independent ripple oscillators are phase-locked by simultaneous activation, related to Figure 7

(**A-B**) Simultaneous multi-site illumination generates phase-coherent iHFOs at higher amplitude (and lower frequency) as compared to sequential, single-site illumination (see also **Figure 7Aa**). (**A**) Wide band (1-5000 Hz) traces from the center of the CA1 pyramidal layer in a freely-moving rat (CaMKII::ChR2) during sequential (single-site at a time, left) and same-intensity simultaneous, multi-site (right) illumination. The time of illumination is indicated by colored bars at bottom, and 470 nm light intensity [mW/mm^2] is indicated below the schematic of each shank. (**B**) Identical experiment in a urethane-anesthetized mouse. Left: Spectrograms show time-frequency decomposition of the pyramidal layer LFP trace (averages of 125 single-site and 61 multi-site pulses). Calibration bars: 20 ms. White numbers indicate the blue-red color-code scaling (single-site power scaled by spontaneous power; multi-site scaled by single-site). For instance, S1 single-site illumination generates local iHFOs with peak power 4 times higher than spontaneous ripples, and multi-site illumination generates S1 iHFOs 2.9 times higher (i.e., 11.6 times the power of spontaneous ripples at the same site). Right: Auto-correlation (same site) and cross-correlation (distant-sites: separation>400 μm) of LFP traces. Bands: mean±SEM.

(**C**) PYR spiking precedes INT spiking during all HFOs (spontaneous ripples, or HFOs induced by single/multi-site illumination). Polar plots show the preferred phases of the same PYR (red dots) and INT (blue) recorded from four freely-moving CaMKII::ChR2 mice during single-shank and multi-shank illumination (see also **Figure 7E**). Large dots indicate the preferred phase of phase-modulated units (Rayleigh test, $p<0.05$) and colored lines show mean phase of those units.

Table S1. List of animals, related to Figure 2

ID	S[1]	Genetics[2-3]	Virus[4-7]	Opsins	Prep[8]	Probe[9-10]	Light sources[11-13]	Sys[14]	Reg[15]	Units[16]	Sess[18]	Misc
30	R	WT[2]	CAG-ChR2[5]	CAG::ChR2	FM	Buzsaki64sp[9]	3 x 470 nm LEDs[11] 2 x SM fibers[12]	RC	DG,CA3	34	1	
31	R	WT	CAG-ChR2	CAG::ChR2	FM	Buzsaki64sp	6 x 470 LEDs	RC	DG,CA3	72	4	
32	R	WT	CAG-ChR2	CAG::ChR2	FM	Buzsaki32	4 x 470 nm LEDs	RC	-	3	1	Few U
47	R	WT	CaMKII-ChR2[6]	CaMKII::ChR2	FM	Buzsaki64sp	6 x 470 nm LEDs	RC	CX,DG	151	5	
52	R	WT	CaMKII-ChR2	CaMKII::ChR2	FM	Buzsaki64sp	6 x 470 nm LEDs	RC	CX	0	2	No U
100	M	CaMKII-Cre[2];Ai35[3]	-	CaMKII::Arch	UA	Buzsaki32[9]	1 x 639 nm LD[11] 2 x MM[12] fibers	AP	CX	90	2	
101	M	CaMKII-Cre;Ai35	-	CaMKII::Arch	UA	Buzsaki32	1 x 639 nm LD 2 x MM fibers	AP	CX	115	3	
201	M	PV-Cre[2];Ai39[3]	-	PV::Halo	UA	Buzsaki32	1 x 639 nm LD 2 x MM fibers	AP	CX	101	2	
258	M	PV-Cre;Ai32[3]	-	PV::ChR2	FM	Buzsaki32	4 x 470 nm LEDs	RC	CX,CA3	87	3	
260	M	PV-Cre;Ai32	-	PV::ChR2	UA	Buzsaki64sp	6 x 470 nm LEDs	RC	CX	16	1	
331	M	PV-Cre	CaMKII-ChR2 DIO-Halo3[7]	CaMKII::ChR2 PV::Halo	FM	Buzsaki32	2 x 470 nm LEDs 2 x 405/660 nm LDs[11]	RC	CX,DG	56	4	
361	M	PV-Cre;Ai32	-	PV::ChR2	FM	Buzsaki32	4 x 470 nm LEDs	RC	CX,CA3	39	3	
365	M	PV-Cre;Ai32	-	PV::ChR2	FM	Buzsaki32	4 x 470 nm LEDs	RC	CX	361	17	
399	M	PV-Cre;Ai32	-	PV::ChR2	FM	Buzsaki32	4 x 470 nm LEDs	RC	CX,CA3	22	4	Few R
401	M	PV-Cre;Ai32	-	PV::ChR2	FM	A1-32-edge[10]	2 x 405 nm LDs[11]	RC	CX,CA3	54[17]	12	
428	M	CaMKII-Cre;Ai32	-	CaMKII:ChR2	FM	Buzsaki32	4 x 470 nm LEDs	RC	CX	150	4	
482	M	PV-Cre;Ai39	CaMKII-ChR2	CaMKII::ChR2 PV::Halo	FM	Buzsaki32	2 x 470 nm LEDs 2 x 405/660 nm LDs	RC	CX,DG	128	4	
483	M	PV-Cre;Ai39	CaMKII-ChR2	CaMKII::ChR2 PV::Halo	FM	A1-32/50[10]	2 x 405/660 nm LDs	RC	CX	2	2	Few U
520	M	PV-Cre;Ai39	-	PV::Halo	FM	A1-32/100[10]	1 x 639 nm LD	RC	CX,CA3	31	8	
531	M	PV-Cre;Ai32	-	PV::ChR2	FM	Buzsaki32	4 x 470 nm LEDs	RC	CX	259	13	
538	M	PV-Cre;Ai32	-	PV::ChR2	UA	Buzsaki64sp	6 x 470 nm LEDs	RC	-	88	1	
552	M	CaMKII-Cre;Ai32	-	CaMKII:ChR2	FM	Buzsaki32	4 x 470 nm LEDs	RC	CX	188	13	
558	M	CaMKII-Cre;Ai32	-	CaMKII::ChR2	FM	A1-32/100	1 x 470 nm LED 1 x MM fiber	RC	CX,CA3	0	6	No U
596	M	PV-Cre;Ai39	-	PV::Halo	FM	Buzsaki32	1 x 639 nm LD	RC	CX	120	6	

							2 x MM fibers					
617	M	PV-Cre;Ai32	-	PV::ChR2	UA	Buzsaki64sp	6 x 470 nm LEDs	RC	-	71	2	
622	M	CaMKII-Cre;Ai32	-	CaMKII::ChR2	UA	Buzsaki64sp	6 x 470 nm LEDs	AP	-	84	2	
624	M	CaMKII-Cre;Ai32	-	CaMKII::ChR2	UA	Buzsaki64sp	6 x 470 nm LEDs	AP	-	60	2	
629	M	CaMKII-Cre;Ai32	-	CaMKII::ChR2	UA	Buzsaki64sp	6 x 470 nm LEDs	AP	-	53	1	
649	M	PV-Cre;Ai32	-	PV::ChR2	FM	Buzsaki32	4 x 470 nm LEDs	RC	CX	318	8	
660	M	PV-Cre;Ai32	-	PV::ChR2	UA	Buzsaki64sp	6 x 470 nm LEDs	RC	-	51	2	
671	M	PV-Cre;Ai32	-	PV::ChR2	UA	Buzsaki64sp	6 x 470 nm LEDs	RC	-	46	1	
705	M	PV-Cre	CaMKII-ChR2 DIO-Arch3[7]	CaMKII::ChR2 PV::Arch	UA	Buzsaki32	1 x 639 nm LD 2 x MM fibers	AP	CX	98	3	
706	M	PV-Cre	CaMKII-ChR2 DIO-Arch3	CaMKII::ChR2 PV::Arch	UA	Buzsaki32	1 x 639 nm LD 2 x MM fibers	AP	-	30	2	
731	M	PV-Cre;Ai32	-	PV::ChR2	UA	Buzsaki32	1 x 639 nm LD 2 x MM fibers	AP	CX	33	1	
763	M	CaMKII-Cre;Ai32	-	CaMKII::ChR2	UA	Buzsaki64sp	6 x 470 nm LEDs	AP	-	51	2	
765	M	CaMKII-Cre;Ai32	-	CaMKII::ChR2	UA	Buzsaki64sp	6 x 470 nm LEDs	AP	-	63	1	
807	M	SOM-Cre[2];Ai32	-	SOM::ChR2	FM	Buzsaki32	1 x 100 µm MM fiber	AP	-	15	2	
808	M	SOM-Cre;Ai32	-	SOM::ChR2	FM	2xBuzsaki32	1 x 100 µm MM fiber	AP	-	33	1	
809	M	SOM-Cre;Ai32	-	SOM::ChR2	FM	2xBuzsaki32	1 x 100 µm MM fiber	AP	-	89	2	
P1	M	PV-Cre	DIO-Halo[7]	PV::Halo	HF	Buzsaki64[9]	4 x SM fibers[13]	NL	-	118	1	
P2	M	PV-Cre	DIO-Halo	PV::Halo	HF	Buzsaki64	4 x SM fibers	NL	-	104	1	Few R
P3	M	PV-Cre	DIO-Halo	PV::Halo	HF	Buzsaki64	4 x SM fibers	NL	-	48	1	Few R
P4	M	PV-Cre	DIO-Halo	PV::Halo	HF	Buzsaki64	4 x SM fibers	NL	-	100	1	Few R
S2	M	SOM-Cre	DIO-Halo	SOM::Halo	HF	Buzsaki64	4 x SM fibers	NL	-	41	1	
S4	M	SOM-Cre	DIO-Halo	SOM::Halo	HF	Buzsaki64	4 x SM fibers	NL	-	55	1	
S5	M	SOM-Cre	DIO-Halo	SOM::Halo	HF	Buzsaki64	4 x SM fibers	NL	-	37	1	
S6	M	SOM-Cre	DIO-Halo	SOM::Halo	HF	Buzsaki64	4 x SM fibers	NL	-	111	1	

1. S=species; R=Rat (300-500 gr); M=Mouse (22-44 gr)

2. WT=Long-Evans male rats (Charles River); SOM-Cre=Sst$^{tm2.1(cre)Zjh}$/J (female; Jackson Labs); CaMKII-Cre=B6.Cg-Tg(Camk2a-cre)T29-1Stl/J (female; Jackson Labs #005359); PV-Cre=B6;129P2-Pvalb$^{tm2.1(cre)Arbr}$/J (female; Jackson Labs #008069)

3. Ai32=B6;129S-Gt(ROSA)26Sor$^{tm32(CAG-COP4*H134R/EYFP)Hze}$/J (ChR2; male; Jackson Labs #012569); Ai35=B6;129S-Gt(ROSA)26Sor$^{tm35.1(CAG-aop3/GFP)Hze}$/J (Arch; male; Jackson Labs #012735); Ai39=B6;129S-Gt(ROSA)26Sor $^{tm39(CAG-hop/EYFP)Hze}$/J (Halo3; male; Jackson Labs #014539) (Madisen et al., 2012)

4. Injection site: rats: PA -3.3±0.5 and ML 3.0±0.5 mm (DV: CX, 1.5±0.2; CA1, 2.2±0.2; CA3, 3.3±0.2; Stark et al., 2012); mice: PA -1.6 and ML 1.1 mm (DV: CX, 0.7±0.2 mm; CA1, 1.1±0.2 mm; CA3: Stark et al., 2013); 55

nl/site; right hemisphere in all animals.

5. CAG-ChR2=rAAV2/5 CAG-ChR2-tdTomato (viral titer estimated at $1x10^{12}$ IU/ml; Janelia Farm Research Campus, Howard Hughes Medical Institute; courtesy of Dr. Svoboda) or rAAV5 CAG-ChR2-GFP (viral titer estimated at $4x10^{12}$ IU/ml; University of North Carolina viral core facility; courtesy of Dr. Boyden)

6. CaMKII-ChR2=rAAV5/CaMKIIa-hChR2(h134R)-EYFP (viral titer estimated at $4x10^{12}$ IU/ml; University of North Carolina viral core facility; courtesy of Dr. Deisseroth)

7. DIO-Halo=Cre-dependent eNpHR-sfGFP (Royer et al., 2012); DIO-Halo3=AAV-EFIa-DIO-eNpHR 3.0-EYFP (courtesy of Dr. Deisseroth); DIO-Arch3=pAAV-Efla-DIO-eArch 3.0-EYFP (courtesy of Dr. Deisseroth)

8. Prep=preparation; FM=freely-moving; HF=head-fixed; UA=urethane-anesthetized

9. Dense probes (20 µm spacing, NeuroNexus): Buzsaki64sp: 6x10 (shanks x sites/shank). Buzsaki64: 8x8; Buzsaki32: 4x8

10. Linear probes: A1-32-edge: sites at edge, 100 µm spacing; A1-32: sites at center; 50/100 µm spacing

11. 470 nm LED=LB P4SG, Osram; 639 nm LD=HL6359MG, Opnext; 405/660 nm LD=SLD6562TL, Sony; 405 nm LD=KES-410ACA, Sony

12. SM/MM-fiber: single-mode fiber (460HP, Thorlabs) or 50 µm multi-mode fiber (AFS50/125, Thorlabs), etched to a point on one side (Stark et al., 2012), fit with an LC connector on the other side (86024-5500, Thorlabs; Royer et al., 2010), and connected via a 5m custom cable (jacket: FT900SM; core: 460HP or AFS105/125; Thorlabs) to an on-bench DPSSL (473 nm/50 mW, Dream Lasers, China; 593 nm/100 mW, Dream Lasers, China; or 473/561 nm, 80/50 mW LightHUB, Omicron, Germany)

13. 4 x SM fibers=4 single-mode fibers (460 HP) coupled via a beam splitter to a common on-bench 561 nm DPSSL (100 mW, Crystalaser; Royer et al., 2012)

14. Sys=recording system. RC (RC Electronics): 1-5000 Hz filter (RC Electronics), 20x (HST/32V-G20, Plexon) and 50x (RC Electronics) amplification, 16 bit, 20 kHz digitization (DataMax, RC Electronics); AP (AmpliPex): 0.3-10,000 Hz filter, 400x amplification (RHA2132, Intan), 14 bit, 20 kHz digitization (KJE-1001, AmpliPex); NL (NeuraLynx): 1-9000 Hz filter, 20x amplification (HST/32V-G20 headstage, Plexon), and 24 bit, 32.552 kHz digitization (Digital Lynx 16SX, NeuraLynx).

15. Reg=additional regions recorded from (CA1 pyramidal layer was monitored in all animals)

16. Units=number of well-isolated CA1 units (units from other regions are not included in this table)

17. Pyramidal layer unit isolation quality is reduced in linear probes (typically only one site in layer)

18. Sess=number of recording sessions

SUPPLEMENTAL EXPERIMENTAL PROCEDURES

Animal procedures

We recorded the activity of multiple single-units and local field potentials (LFP) from CA1 of five freely-moving rats (300-500 gr, 2-4 month old males) and 42 mice (18 freely-moving, 8 head-fixed, and 16 urethane-anesthetized; 22-44 gr, 2-6 month old males and one 36 gr 4 month old female) as previously described (Royer et al., 2012; Stark et al., 2012; Stark et al., 2013). After the initial surgery, animals were kept one to a cage on a reversed light/dark cycle. All animal handling procedures were approved by the Rutgers University and New York University Animal Care and Facilities committees. **Table S1** lists the animals used in this study and summarizes the techniques employed. We used transgenic mice (Madisen et al., 2012), virus injections (Stark et al., 2012), or a combination of both, in order to obtain expression of exogenous light-sensitive opsins in behaving rodents. Animals expressed channelrhodopsin-2 (ChR2; Boyden et al., 2005), halorhodopsin-3 (Halo; Gradinaru et al., 2010), and/or archaerhodopsin-3 (Arch; Chow et al., 2010; Mattis et al., 2012) under the CAG, CaMKII, PV, and/or SOM promoters. All animals were implanted with silicon probes (NeuroNexus) on movable microdrives. One or more optical fibers were attached to the probe shanks (Royer et al., 2010), terminating in a tip etched to a point above electrode sites. At the other end, fibers were coupled to diodes (Stark et al., 2012; 470 nm blue light-emitting diode, LED; or 639/660 nm red laser diode, LD; or 405 nm violet LD) or terminated with an LC connector (Royet et al., 2010) for tethering to an external diode-pumped solid state laser (DPSSL). Freely-moving animals were implanted with linear probes (n=4 mice; tip in str. radiatum) or with high-density probes (32 or 64 sites; n=14 mice and n=5 rats; tips in neocortex) and moved gradually (≤70 μm/day). Peak light power, measured at the tip of the shanks before implantation, was: 29±12 μW (mean±SD; n=68 470 nm LEDs), 239±61 μW (n=7 405 nm LDs), 395±167 μW (n=3 639 nm LDs and n=4 660 nm LDs). For DPSSL-driven stimulation, peak light power measured at the end of the fiber was about ten times higher (473 nm: 3-17 mW; 561 nm: 1-12 mW; and 593 nm: 6-10 mW).

Recording procedures and feed-forward stimulation experiments

Neural activity was wide-band filtered (high-pass: 0.3 Hz or 1 Hz; low-pass: 5, 9, or 10 kHz), amplified, and digitized (**Table S1**). Freely-moving animals were equipped with a 3-axis accelerometer (ADXL-330, Analog Devices) for monitoring head-movements, 2 head-mounted LEDs for online video tracking, or both. Recordings from freely-moving animals were carried out in the home cage during spontaneous behavior. After each session the probe was either left in place or advanced in 35-70 μm steps and the brain was allowed to settle overnight. At each location in the brain, neuronal activity was inspected for spontaneous spiking activity, and if encountered, a baseline period of at least 15 minutes was recorded followed by light stimulation.

Photostimulation was performed at each light-equipped shank separately and simultaneously on all light-equipped shanks at the minimal light intensity that evoked an effect detectable by visual inspection during the experiment, and at multiple intensities above and below that level. All stimuli were a-periodic and had either a half-sine (60-120 ms) or a square pulse (50-400 ms) waveform. Initially, half-sine waveforms were employed, designed to mimic the CA3-generated SPW observed in the CA1 str. radiatum (**Figure 2Ba**), and a wide range

of stimulus parameters was tested. iHFOs were readily induced in all configurations including square pulses, but were typically self-limited to 30-50 ms (**Figure 2A**). Therefore in subsequent experiments, square pulses were used for simplicity and specificity.

Pharmacological experiments

To determine if $GABA_A$ receptor-mediated inhibition is critically involved in pacing and/or coordination of CA1 ripples, intra-cortical injection of the $GABA_A$ receptor blocker picrotoxin (PTX) was used. Ideally, a single perturbation should be made at a time, namely, the drug effect on spontaneous ripples should be observed. However, reliably-detectable, high-power ripples occur about once every 2-5 s under anesthesia, while PTX kinetics, and especially the spread of the drug in the intact brain, have faster dynamics. To avoid the problem of low incidence of ripples, iHFOs were induced in urethane-anesthetized CaMKII::ChR2 mice. Light stimulation (50 ms pulses) was delivered either sequentially (one shank at a time) or simultaneously (together on all shanks), at two intensities: the site-specific threshold for iHFO generation, and double that intensity. A complete cycle of stimulating 6 shanks lasted 10 s, and 30 such repetitions (120 pulses/shank) were applied to obtain a baseline. PTX (Tocris; 1 mM in PBS; 13-52 nl, 26 nl/s) was then injected (pipette tip diameter, 30-50 µm; held by Nanoject II, Drummond) approximately 50-100 µm from one of the recording shanks while repeating the stimulation with the same parameters.

Histology

Mice and rats were anesthetized with pentobarbital injection (100 mg/kg) and perfused with saline and 4% paraformaldehyde before their brains were rapidly removed. Coronal sections (50 or 80 µm) were cut on a vibratome (Leica, VT1000S) and collected in phosphate buffered saline (PBS). After 3 washes in PBS (10 min each), sections were permeabilized and blocked in PBS containing 10% normal goat serum and 0.2% Triton-X100 (PBS*) for 1 hour and processed for immunostaining by overnight incubation at 4°C with primary antibodies diluted in PBS*. The primary antibodies used in this study were the following: monoclonal mouse anti-alpha-CaM Kinase II (1:500; 13-7300, Invitrogen), polyclonal rabbit anti-parvalbumin (1:1000; PV 25, Swant), and polycloncal rabbit anti-somatostatin (1:500; LS-C172192, LifeSpan Biosciences). After 2 washes (30 min each) in PBS*, sections were incubated for 2 hours at room temperature with secondary antibodies diluted in PBS* (goat anti-rabbit IgGs conjugated to Alexa Fluor 555 dyes; 1:3000; A-21428, Molecular Probes). After 2 washes (20 min each), sections were incubated for 20 min in PBS containing DAPI (1:10000; D1306, Molecular Probes), and washed again 3 times (10 min each) in PBS. Sections were mounted in Fluoromount (Sigma) and imaged with a wide-field fluorescence microscope (Zeiss, Axioscope) or a confocal laser-scanning microscope (Zeiss, LSM 700).

Spike detection, sorting, and cell-type classification

For offline analysis, spike waveforms were extracted from the wide-band recorded signals. Waveforms were linearly detrended, projected onto a common basis obtained by principal component analysis of the data, and sorted automatically (Harris et al., 2000) followed by manual adjustment. Only well-isolated units (amplitude >50 µV; L-ratio <0.05, Schmitzer-Torbert, 2005; ISI index <0.2, Fee et al., 1996) were used. Subsequently each unit was tagged as excitatory/inhibitory (based on peaks/troughs in the short-time [±5 ms] pair-wise

cross correlation; p<0.001, convolution test; Stark and Abeles, 2009), tagged as PV/SOM (based on spiking response to light; p<0.001, Poisson test), or classified as putative PYR or INT (based on a Gaussian-mixture model, Stark et al., 2013; p<0.05). We recorded a total of 3885 well-isolated cells from CA1 of 5 freely-moving rats and 42 mice (**Table S1**). Of these, 2959 were PYR and 870 were INT (of these, 184 were optically-tagged PV cells and 29 optically-tagged SOM cells; the rest were untagged INT). 56 well-isolated units were not classified.

Statistical testing

For a given effect size, the power of any statistical test depends on the α level. To increase the sensitivity of detecting effects, results are reported based on a significance threshold α=0.05, and all groups included enough samples to enable rejection of the null at that level. Non-parametric testing was used in all cases: Wilcoxon's signed-rank test (two-sided for paired testing; one-sided for a zero- or unity null) and Mann-Whitney U-test (two-sided; for comparing the medians of unpaired groups). An exception to this was the F-test used to assess the significance of coherence. Circular (or circular-linear) measures were tested using the χ^2 test. All results were verified independently by resampling (permutation) tests.

Ripple-associated spike timing histograms

The instantaneous phase of the DOG-filtered signal was derived from its Hilbert transform, and spikes that occurred during a ripple event were assigned the phase (0-2π) at the time of firing. For spontaneous ripples (i.e., whose onset did not overlap with any light stimulus), the phase of each spike was shifted by an integer multiple of 2π, such that phase π corresponded to the LFP trough closest to the peak ripple power, 3π to the trough of the second cycle, etc. For induced oscillations (i.e., whose onset overlapped with a light stimulus), the stimulus onset was used as the reference point for spike phase warping (i.e., the first LFP trough following the onset was assigned phase π etc). Note that only spikes that occurred during a (spontaneous or induced) HFO event were assigned phases.

For each unit, three types of spike timing histograms were generated, each chosen to highlight different ripple-associated properties of spiking: (1) time-domain PSTH, triggered by the time of the peak ripple power (trough-aligned to peak power for spontaneous events or to stimulus onset for induced events; optimized for time locking to a single point in time; **Figure 5** and **Figure S5**); (2) ripple-duration warped PSTH, triggered by the ripple peak, but partitioned into 8 intra-ripple and 24 peri-ripple bins (Klausberger et al., 2003; optimized for time locking to an event of potentially variable duration; **Figure S1**); (3) phase-domain PSTH, triggered by the ripple peak (this included only spikes that were assigned a phase; optimized for displaying temporal dynamics in relation to an oscillation of potentially-variable frequency; **Figure 3** and **Figure S3**).

SUPPLEMENTAL REFERENCES

Boyden, E.S., Zhang, F., Bamberg, E., Nagel, G., and Deisseroth, K. (2005). Millisecond-timescale, genetically targeted optical control of neural activity. Nat. Neurosci. 8, 1263-1268.

Chow, B.Y., Han, X., Dobry, A.S., Qian, X., Chuong, A.S., Li, M., Henninger, M.A., Belfort,

G.M., Lin, Y., Monahan, P.E., and Boyden, E.S. (2010). High-performance genetically targetable optical neural silencing by light-driven proton pumps. Nature 463, 98-102.

Fee, M.S., Mitra, P.P., and Kleinfeld, D. (1996). Automatic sorting of multiple unit neuronal signals in the presence of anisotropic and non-Gaussian variability. J. Neurosci. Methods 69, 175-188.

Gradinaru, V., Zhang, F., Ramakrishnan, C., Mattis, J., Prakash, R., Diester, I., Goshen, I., Thompson, K.R., and Deisseroth, K. (2010). Molecular and cellular approaches for diversifying and extending optogenetics. Cell 141, 154-165.

Harris, K.D., Henze, D.A., Csicsvari, J., Hirase, H., and Buzsáki, G. (2000). Accuracy of tetrode spike separation as determined by simultaneous intracellular and extracellular measurements. J. Neurophysiol. 84, 401-414.

Madisen, L., Mao, T., Koch, H., Zhuo, J.M., Berenyi, A., Fujisawa, S., Hsu, Y.W., Garcia, A.J. 3rd, Gu, X., Zanella, S., Kidney, J., Gu, H., Mao, Y., Hooks, B.M., Boyden, E.S., Buzsáki, G., Ramirez, J.M., Jones, A.R., Svoboda, K., Han, X., Turner, E.E., and Zeng, H. (2012). A toolbox of Cre-dependent optogenetic transgenic mice for light-induced activation and silencing. Nat. Neurosci. 15, 793-802.

Mattis, J., Tye, K.M., Ferenczi, E.A., Ramakrishnan, C., O'Shea, D.J., Prakash, R., Gunaydin, L.A., Hyun, M., Fenno, L.E., Gradinaru, V., Yizhar, O., and Deisseroth, K. (2012). Principles for applying optogenetic tools derived from direct comparative analysis of microbial opsins. Nat. Methods 9, 159-172.

Royer, S., Zemelman, B.V., Barbic, M., Losonczy, A., Buzsáki, G., and Magee, J.C. (2010). Multi-array silicon probes with integrated optical fibers: light-assisted perturbation and recording of local neural circuits in the behaving animal. Eur. J. Neurosci. 31, 2279-2291.

Royer, S., Zemelman, B.V., Losonczy. A., Kim, J., Chance, F., Magee, J.C., and Buzsáki, G. (2012). Control of timing, rate and bursts of hippocampal place cells by dendritic and somatic inhibition. Nat. Neurosci. 15, 769-775.

Schmitzer-Torbert, N., Jackson, J., Henze, D., Harris, K., and Redish, A.D. (1996). Quantitative measures of cluster quality for use in extracellular recordings. Neuroscience 131, 1-11.

Stark., E., and Abeles M. (2009). Unbiased estimation of precise temporal correlations between spike trains. J. Neurosci. Methods 179, 90-100.